Dynamically isotropic Gough-Stewart platform for micro-vibration isolation in spacecrafts

Yogesh Pratap Singh[a], Nazeer Ahmad[b], Ashitava Ghosal[a,*]

[a] *Department of Mechanical Engineering, Indian Institute of Science, Bangalore, 560012, India*
[b] *URSC, Indian Space Research Organization, Bangalore, 560017, India*

Abstract

This paper deals with the modeling, simulation, and experimental validation of a modified Gough-Stewart platform (MGSP) for vibration isolation, where the first six natural frequencies corresponding to the first six degree-of-freedom are nearly the same, enabling effective attenuation of the first six modes. The configuration is termed as dynamically isotropic and this work presents a geometry-based analytical approach to obtain the design parameters of the MGSP at its neutral position. The approach accommodates various payload configurations, including variable center of mass and mass/inertia properties. The validation of the design is demonstrated using a finite element software ANSYS®, and the model is further refined to incorporate flexural joints and structural damping. A prototype of the MGSP featuring flexural joints was tested, and it yielded experimental outcomes in close agreement with the finite element analysis results – the first six natural frequencies were close to the expected 29 Hz and vibration isolation of about 22 dB/octave. The close agreement among analytical, finite element, and experimental outcomes underscores the efficacy of our design approach and the suitability of an MGSP for micro-vibration isolation applications in spacecraft.

Keywords: Dynamic isotropy, Modified Gough-Stewart Platform, Natural Frequency, Damping, Vibration isolation

*Corresponding author
Email addresses: yogeshsingh@iisc.ac.in (Yogesh Pratap Singh), asitava@iisc.ac.in (Ashitava Ghosal)

1. Introduction

Rotating elements in reaction wheels, momentum wheels, and gimbal antennas, as well as reciprocating subsystems in cryocoolers, induce vibration on spacecraft during on-orbit operations [1]. These in-orbit low amplitude micro-vibrations, occurring within a bandwidth of 250 Hz, adversely affect the performance of optical payloads such as imagers/cameras and inter-satellite communication links mounted on the spacecraft bus [1, 2, 3]. To mitigate these disturbances, isolators can be integrated between the spacecraft and the noise sources. Furthermore, spacecraft experience intense vibrations and shock environments during launch, with frequencies below 100 Hz and a high quasi-static load of around $10g$ [1, 4]. This demands an isolation system capable of handling both low-amplitude, multi-directional vibrations during orbit and high-amplitude vibrations during launch.

Typically, the first six modes (three translation and three rotational) contain most of the vibrational energy, and an effective vibration isolation system needs to attenuate all six modes corresponding to the first six degrees of freedom (DOF) equally. Numerous studies have investigated cubic configuration [5, 6, 7] and other variants of Gough-Stewart Platform (GSP) [8] based vibration isolators to achieve the desired vibration isolation. Consequently, researchers have proposed decoupled and isotropic measures to enhance performance [9, 10]. In recent years, significant research efforts have gone into design and control of aspects of GSPs, such as orthogonality [10, 11], kinematic isotropy [12, 13], stiffness isotropy [14] and static isotropy [15, 16]. Most research on vibration isolation using GSPs has focused on employing active control within a cubic architecture [5, 6, 7]. This preference arises because the cubic architecture possess the attractive decoupling characteristics. However, in these designs, the different natural frequency peaks of first six DOF modes could affect isolator performance due to coupling of the cross DOFs as depicted schematically in Fig. 1a [17] – the vibration isolation region for the $\boldsymbol{X}$ mode (beyond $\sqrt{2}\omega$) is affected by the natural frequency peaks of the $\boldsymbol{Z}$ and the Rot ($\boldsymbol{X}$) modes. As a result, effective vibration isolation for the three modes depicted in Fig.1a cannot be achieved. Similar challenge arises in designing GSPs, with different natural frequencies, for vibration isolation purposes. While kinematic or static isotropy in GSPs is effective for precise pointing applications [9], it is not ideal for passive vibration isolation because the resonance peaks are not aligned – the kinematic isotropic GSP designed in [9] for precise pointing applications has six natural frequencies:

80.4, 80.4, 80.4, 50.8, 50.8, and 35.9 Hz. This configuration implies that the isolation region associated with the mode at 35.9 Hz is impacted by the resonance peaks of the other modes.

Dynamic isotropy, with the first six natural frequencies corresponding to the first six DOFs nearly equal, is a crucial design consideration [18, 19, 20], and it ensures that resonance peaks are aligned. The benefits of dynamic isotropy over other types of isotropies (stiffness, force, and velocity isotropies) stem from its dependence on the payload's mass center and inertia properties, along with geometric and stiffness parameters. The dynamic isotropy configuration can simplify damper tuning in passive vibration control and identical dampers can be used in the legs of the GSP [21]. From an active control perspective, a multi-input-multi-output (MIMO) system can be treated as several single-input-single-output (SISO) systems, allowing for a decoupled control strategy in an isotropic design [9, 21, 22] – in a non-isotropic and coupled design, the coupling among all six DOFs of the GSP complicates controller design, leading to a reduction in control accuracy [9]. Active control systems possess the capability to fulfill both fundamental vibration control requirements: low amplification at resonances and a high roll-off rate in the isolation region. However, active control systems necessitate electronic systems for signal processing and significant computational capacity for real-time computation, resulting in increased spacecraft mass and power requirements. Therefore, designing a passive vibration isolation system based on a dynamically isotropic GSP is advantageous. This approach provides uniform damping while addressing the critical considerations of mass and power requirements in spacecraft applications. Furthermore, a dynamically isotropic GSP also provides stability information, as the lowest natural frequency significantly influences dynamic stability [23]. Ensuring nearly equal natural frequencies also maximizes the lowest natural frequency, which is favorable for stability. Additionally, an isotropic manipulator excels in kinematic accuracy and avoids singular configurations [12].

Previous research on decoupling or achieving dynamic isotropy has primarily focused on a 6-6 Gough Stewart Platforms (GSP) [8, 18, 21, 22]. The literature highlights that a conventional GSP or standard GSP (SGSP) lacks static isotropy [15] and dynamic isotropy [18]. Achieving dynamic isotropy with an SGSP is practically challenging due to restrictions in meeting inertia conditions. Specifically, the Z component of inertia (I_{ZZ}) needs to be four times the X and Y components ($I_{XX} = I_{YY}$) [18]. Dynamic isotropy can be attained using a two-radii GSP or a modified GSP (MGSP) [20, 24, 25]. As

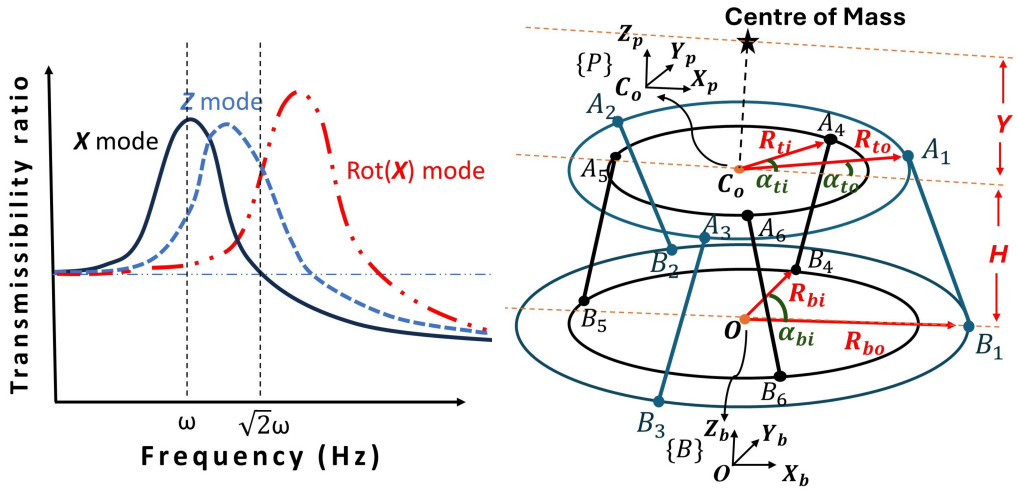

(a) (b)

Figure 1: **a)** Transmissibility curve for a non-isotropic design, **b)** Modified Gough Stewart platform (MGSP)

the name implies, unlike in the conventional 6-6 GSP where anchor points lie on a single radius, in the two-radii GSP or MGSP, the anchor points are distributed on two radii on each platform, as illustrated in Fig. 1b. The additional design variables (two radius and two angles) in an MGSP, compared to a conventional GSP, provide greater design flexibility and enables a design for dynamic isotropy.

Yi et al. [10] developed techniques for generating locally orthogonal and isotropic classes of modified GSPs. However, these designs do not address dynamic isotropy, which is crucial for effective vibration isolation design. Tong et al. [24] attempted to streamline analytical solutions to accommodate various mass center requirements and employed particle swarm optimizations to ensure optimal outcomes, but the solutions weren't expressed in straightforward explicit forms, which could complicate their practical implementation. Jiang et al. [25] utilized a pair of circular hyperboloids to characterize a modified GSP (MGSP), exploring the correlation between dynamic isotropy and the geometric parameters of the hyperboloids. However, the study didn't provide general closed-form solutions, which limited their applicability to a wider range of scenarios. The designing of dynamically isotropic MGSPs from previous studies remains challenging as solutions are often implicit or intertwined, lacking flexibility and feasibility regarding space constraints or

leg intersections in 3D space. In an earlier work [26], a partially dynamic isotropic design, ignoring the torsional mode, was presented for an MGSP.

In this work, we derive the analytical solution for the design parameters of a dynamically isotropic MGSP in closed-form. The 3-dimensional dynamically isotropic MGSP problem was transformed into a two-dimensional geometry problem involving a pair of triangles with certain geometrical relationships, and closed-form expressions involving the design variables were obtained. While many existing works overlook the variation in the center of mass (COM) from the mobile platform, our geometry-based design approach takes into account the practicality of incorporating the general case of COM variation. The results obtained from the geometry-based approach are validated using a finite element (FE) model in ANSYS®, revealing uniform natural frequencies across all the first six modes. Subsequently, we enhanced the model to incorporate damping and flexural joints to address issues related to friction, backlash errors, and lubrication associated with conventional joints, which is especially pertinent in spacecraft applications [5, 7, 9]. The FE model with flexural joints are in reasonable agreement with the analytical formulation's results – the difference is mainly due to the introduction of parasitic stiffness at the flexural joints. An MGSP with flexural joints was developed at the Indian Space Research Organization (ISRO), and experimental findings are closely aligned with the FEM and analytical results. The analytical formulation is modified to include damping in the legs of an MGSP, and the damping values obtained from FE and experimental methods are used to validate our approach and assess the dynamic performance of the dynamically isotropic MGSP. To the best of our knowledge, for the first time, this work presents a detailed methodology for designing a dynamic isotropic MGSP tailored to specific applications. Furthermore, none of the previous studies have experimentally demonstrated dynamic isotropy in an MGSP.

This paper is organized as follows: in Section 2, we present the analytical formulation to obtain the design parameters of the MGSP. Section 3 presents the design methodology for a desired requirement, Section 4 presents a validation of the analytical formulation using an FE model, and Section 5 presents the experimental setup on MGSP for vibration isolation. Section 6 presents the results of the experiments and a discussion on the comparison of the results obtained from the analytical, finite element model and experiments. An analytical damping model consistent with our FE and experimental results is developed. Finally, Section 7 presents the conclusion and scope for future

work in this area.

2. Analytical Formulation

A Modified Gough-Stewart Platform (MGSP) is a 6-DOF parallel manipulator consisting of a mobile platform, a fixed base, and six legs with prismatic joints connecting these two platforms, as shown in Fig. 1b. Each leg of MGSP is connected to the mobile platform through a spherical joint and to the base platform through a spherical or universal joint. The anchor points A_1 to A_6 are located on two radii represented by variables R_{ti} (inner) and R_{to} (outer) with center C_o. Similarly, the points B_1 to B_6 are located on two radii on the base platform represented by R_{bi} (inner) and R_{bo} (outer) with center O. There are two different sets of three identical legs with equal angular spacing of 120° along the circumference of each radius. The variable H denotes the height between the two platforms in its neutral configuration where both platforms are parallel to each other. The variable Y denotes the height of the payload's COM from the movable platform. The coordinates of any point expressed in the base frame $\{B\}$ are represented by $\{x_b, y_b, z_b\}$ and on the moving frame $\{P\}$ are represented by $\{x_p, y_p, z_p\}$. The vector $\boldsymbol{OB_1}$, with magnitude equal to R_{bo}, is chosen along $\boldsymbol{X_b}$. The variable α_{bi}, α_{to}, and α_{ti} denote angles made by vectors $\boldsymbol{OB_4}$, $\boldsymbol{C_oA_1}$, and $\boldsymbol{C_oA_4}$ with vector $\boldsymbol{X_b}$, respectively (see Fig. 1b).

The analytical formulation for the dynamic isotropy in MGSP was derived using the force transformation matrix ($[\mathbf{B}]$) [5, 26, 27], which maps joint space forces to the task space. All legs are assumed to have an equal axial stiffness k in their joint space. Therefore, the stiffness matrix $[\mathbf{K}_T]$ in the task space [5, 28] is given by

$$[\mathbf{K}_T] = k[\mathbf{B}][\mathbf{B}]^T \tag{1}$$

The force transformation matrix ($[\mathbf{B}]$) for MGSP is given by

$$[\mathbf{B}]_{6\times 6} = \begin{bmatrix} \boldsymbol{s_1} & \dots & \boldsymbol{s_6} \\ ({}^B[\mathbf{R}]_P({}^P\boldsymbol{p_1} - {}^P\boldsymbol{H_c})) \times \boldsymbol{s_1} & \dots & ({}^B[\mathbf{R}]_P({}^P\boldsymbol{p_6} - {}^P\boldsymbol{H_c})) \times \boldsymbol{s_6} \end{bmatrix} \tag{2}$$

where $\boldsymbol{s_j} = \dfrac{{}^B\boldsymbol{t} + {}^B[\mathbf{R}]_P\,{}^P\boldsymbol{p_j} - {}^B\boldsymbol{b_j}}{l_j}$, $j = 1, \dots, 6$. The vector $\boldsymbol{S}_j$ $(= l_j \boldsymbol{s}_j)$ is directed along the respective leg of an MGSP with length l_j while ${}^B\boldsymbol{t}$ is a

vector from centre of the base platform to the centre of the mobile platform. The symbols ${}^{P}\boldsymbol{p_j}$ and ${}^{B}\boldsymbol{b_j}$ represent the coordinates of an anchor point on the mobile and base platform expressed in their respective frames. The vector ${}^{P}\boldsymbol{H_c}$ represents the location of the combined COM of the mobile plate and the payload with respect to the mobile platform.

The analytical formulation for MGSP assumes that the MGSP it is at its neutral position. This is a reasonable assumption for a micro-vibration isolation and control application, as there will not be a large motion of the mobile platform. In this neutral configuration, both platforms are parallel (implying ${}^{B}[\mathbf{R}]_{P} = [\mathbf{I}]$), and the payload's COM, the centre of the mobile platform, and the centre of the fixed base lie on the same vertical line (implying ${}^{B}\boldsymbol{t} = [\ 0\ 0\ H\ ]^{T}$ and ${}^{P}\boldsymbol{H_c} = [\ 0\ 0\ Y\ ]^{T}$). The matrix $[\mathbf{B}]$ is constant at this neutral position, and for a given $[\mathbf{B}]$, the connection points are not uniquely determined [10, 18]. This results in different design configurations as presented in Section 3 on the design of dynamically isotropic MGSPs.

The mass matrix $[\mathbf{M}]_{6\times6}$ will have a diagonal form if the orientation of the principal axes of the payload is chosen to coincide with the global coordinate system and is given by:

$$[\mathbf{M}] = \text{diag}[\ m_p,\ m_p,\ m_p,\ I_{xx},\ I_{yy},\ I_{zz}] \tag{3}$$

where m_p represents the mass of the payload (including the mass of the mobile platform) and I_{xx}, I_{yy}, and I_{zz} denotes its principal moment of inertia along $\boldsymbol{X}$, $\boldsymbol{Y}$, and $\boldsymbol{Z}$ directions with respect to its COM. The mass and inertia of the legs are neglected as they are expected to be significantly smaller than the total payload mass being manipulated.

From Eqs. (1), (2) and (3), the natural frequency matrix $[\mathbf{G}]$ in task space [18, 24, 25] can be expressed as

$$[\mathbf{G}] = [\mathbf{M}]^{-1}[\mathbf{K_T}] = [\mathbf{M}]^{-1}k[\mathbf{B}][\mathbf{B}]^{T} = \begin{bmatrix} \mathbf{P} & \mathbf{T} \\ \mathbf{T^T} & \mathbf{U} \end{bmatrix} \tag{4}$$

with $[\mathbf{P}] = \text{diag}(\lambda_1, \lambda_2, \lambda_3)$, $[\mathbf{U}] = \text{diag}(\lambda_4, \lambda_5, \lambda_6)$, $[\mathbf{T}] = \begin{bmatrix} \mu_{11} & -\mu_{12} & 0 \\ \mu_{12} & \mu_{11} & 0 \\ 0 & 0 & \mu_{33} \end{bmatrix}$

The appearance of zero terms in the above matrix $[\mathbf{G}]$ is due to symmetries arising from the equal angular spacing of 120° among the same type of legs. The expressions for λ_i and μ_{ij} in the above equations are given in the

Appendix. The leg length ratio, a, is a variable that relates the lengths of two sets/types of legs by

$$l_{o2} = a\ l_{o1} \tag{5}$$

where, for the first set of legs, $l_{o1} = |\boldsymbol{S_1}| = |\boldsymbol{S_2}| = |\boldsymbol{S_3}|$ and similarly, $l_{o2} = |\boldsymbol{S_4}| = |\boldsymbol{S_5}| = |\boldsymbol{S_6}|$ (detailed expression are given in Appendix).

The obtained matrix $[\mathbf{G}]$ is a function of all the design variables for an MGSP, i.e., R_{bo}, R_{to}, R_{bi}, R_{ti}, H, Y, α_{to}, and $(\alpha_{bi} - \alpha_{ti})$. These design parameters can be obtained by solving the coupled transcendental equations generated by equating the six natural frequencies. The matrix $[\mathbf{G}]$ will become a diagonal matrix if the off-diagonal terms of the matrix $[\mathbf{G}]$ (i.e., $[\mathbf{T}]$) are set to zero, and then the diagonal terms of the $[\mathbf{G}]$ matrix will represent its eigenvalues. For dynamic isotropy of the MGSP at its neutral position, the following condition must be satisfied:

$$\lambda_1 = \lambda_2 = \lambda_3 = \lambda_4 = \lambda_5 = \lambda_6 = \omega^2 \text{ and } \mu_{11} = \mu_{12} = \mu_{33} = 0 \tag{6}$$

where, ω is the natural frequency of the MGSP and λ_1 to λ_6 are the eigenvalues of the matrix $[\mathbf{G}]$. It can be observed from Eq. (4) that the variable λ_1, λ_2 and λ_3 corresponds to $\boldsymbol{X}$, $\boldsymbol{Y}$ and $\boldsymbol{Z}$ DOFs, while variable λ_4, λ_5 and λ_6 corresponds to Rot($\boldsymbol{X}$), Rot($\boldsymbol{Y}$) and Rot($\boldsymbol{Z}$) DOFs, respectively.

3. Design of Dynamically Isotropic MGSP

The design of a dynamically isotropic MGSP involves finding unknown parameters from the known given parameters and free/input variables. In the intended application, the payload properties, such it's mass (m_p), inertia (I_{xx}, I_{yy}, I_{zz}), and centre of mass (COM) height (Y) are known to us. For an axisymmetric wheel-like payload, $I_{xx} = I_{yy}$ implying $\lambda_4 = \lambda_5$ in Eq. (6). For ease of understanding, we will first consider the case when there is no COM variation (Y=0) and then extend our formulation to the practical case of $Y \neq 0$.

3.1. COM on the mobile platform ($Y = 0$)

All the dynamic isotropic conditions mentioned in Eq. (6) were simplified, and results are listed in the second column of Table 1. Figure 2a presents a geometrical interpretation of the simplified results in the second column of Table 1. It can be seen that the 3D MGSP design problem reduces to a

Table 1: Geometrical interpretations of a dynamically isotropic MGSP with $Y = 0$

Case	**Condition used**	**Simplified Equation**	**Geometrical Interpretation in Fig. 2a**
1	$\lambda_1 = \lambda_3$ and Eq. (5)	${b_1}^2 = R_{ti}^2 + R_{bi}^2 - 2R_{ti}R_{bi}\cos(\alpha_{bi} - \alpha_{ti})$	$\Delta Q_o P_1 R_1$:triangle with sides R_{bi}, R_{ti} and b_1 (cosine rule)
2	$\lambda_1 = \lambda_3$ and Eq. (5)	${b_2}^2 = R_{to}^2 + R_{bo}^2 - 2R_{to}R_{bo}\cos(\alpha_{to})$	$\Delta Q_o P_2 R_2$:triangle with sides R_{bo}, R_{to} and b_2
3	$\mu_{11} = 0$	$R_{ti}R_{bi}\sin(\alpha_{bi} - \alpha_{ti}) = a^2 R_{to}R_{bo}\sin(\alpha_{to})$	Area of $\Delta Q_o P_1 R_1 = a^2 \times$ (Area of $\Delta Q_o P_2 R_2$)
4	$\mu_{12} = 0$	$R_{ti}(R_{ti} - R_{bi}\cos(\alpha_{bi} - \alpha_{ti})) = a^2 R_{to}(R_{bo}\cos(\alpha_{to}) - R_{to})$	$(\overline{Q_o R_1})P_{g1} = a^2 (\overline{Q_o R_2})P_{g2}$
5	$\lambda_4 = \lambda_3$ and $\lambda_4 = \lambda_6$	$\frac{a^2 R_{to}^2}{a^2+1} + \frac{R_{ti}^2}{a^2+1} = 2Q$	$\overline{P_3 R_3}$ is a constant magnitude line treating R_{to} and R_{ti} as perpendicular basis.
6	$\mu_{12} = 0$ and $\mu_{11} = 0$	$\tan\theta_1 = \tan\theta_2$	$\angle Q_o R_1 P_1 = 180° - \angle Q_o R_2 P_2 \implies \theta_1 = \theta_2 = \theta$
where $b_1 = H\sqrt{C_1}$, $b_2 = \frac{H\sqrt{C_2}}{a}$, $C_1 = \left(\frac{3a^2+1}{2}\right)$, $C_2 = \left(\frac{a^2+3}{2}\right)$			

set of two triangles in 2D space, as shown in Fig. 2a, and the geometrical interpretations are as listed in the third column of Table 1. The geometrical interpretations greatly simplifies the process of developing closed-form solutions to all the design variables. It is to be noted that the payload properties are expressed in terms of ratios in our expressions as $K(= I_{xx}/I_{zz})$ and $Q(= I_{xx}/m_p)$ while leg length ratio a (refer to Eq. (5)) is taken as free/input variable. The design variable obtained by satisfying the geometrical conditions in Table 1 will represent a dynamically isotropic configuration in MGSP. There can be many such triangle pairs implying multiple solutions, and the choice of triangle pair will be governed by space constraints or dimension requirements. It is, however, challenging to construct a general triangle pair

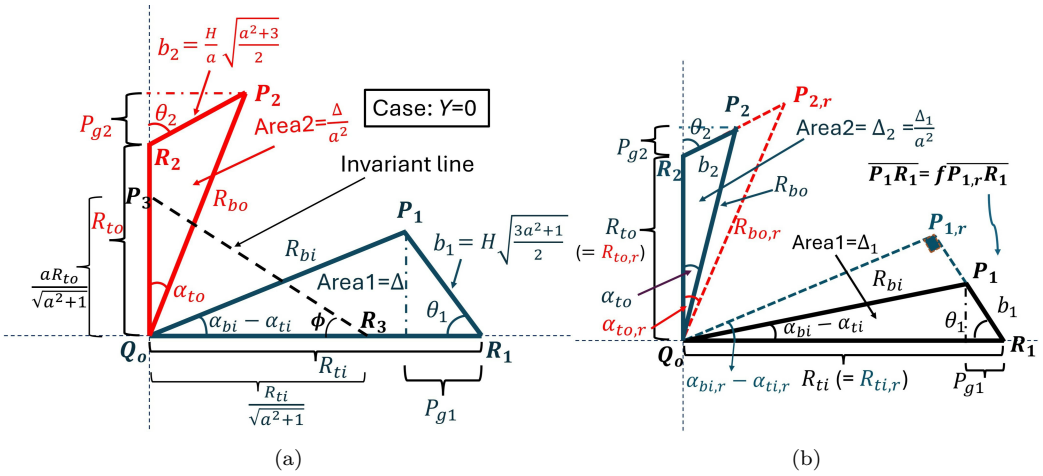

Figure 2: **a)** Geometrical interpretation of Table 1, **b)** General triangle obtained using the corresponding right-angled triangle.

($\Delta Q_o P_1 R_1$ and $\Delta Q_o P_2 R_2$ in Fig. 2a) with geometrical relations that can yield the desired design variables (dimensions) of MGSP. To solve for a general triangle, the corresponding right angle ($\Delta Q_o P_{1,r} R_1$ in Fig. 2b) can be deduced by making use of the Pythagoras theorem. All the parameters denoted by subscript 'r' correspond to the right angle triangle case for a particular triangle pair. It is to be noted that this right-angle triangle ($\Delta Q_o P_{1,r} R_1$) and its triangle pair ($\Delta Q_o P_{2,r} R_2$) also represent one of the dynamical isotropic configuration.

The use of Pythagoras theorem in a right angle triangle ($\Delta Q_o P_{1,r} R_1$) in our previous work (refer to [28]) yielded a set of solutions by solving expression analytically in Eq. (6). Hence, the variables corresponding to this right-angle case are given by:

$$
\begin{aligned}
&R_{ti,r} = \sqrt{QC_2}, R_{to,r} = \frac{\sqrt{QC_1}}{a}, H_r = \sqrt{\frac{Q(KC_1C_2 - a^2)}{KC_1^2}}, \\
&\theta = \arctan\left(\frac{a}{\sqrt{KC_1C_2 - a^2}}\right) \text{and } (\alpha_{bi,r} - \alpha_{ti,r}) = 90^\circ - \theta \\
&R_{bi,r} = \sqrt{\frac{Qa^2}{KC_1}}, \;\; R_{bo,r} = \sqrt{\frac{QC_1}{a^2} + \frac{Q(KC_1C_2 - a^2)(2C_1 + C_2)}{KC_1^2a^2}} \\
&\alpha_{to,r} = \arctan\left(\frac{b_{2r}\;\sin(\theta)}{R_{to} + \;b_{2r}\;\cos(\theta)}\right)
\end{aligned}
\tag{7}
$$

The in-depth analytical development of these expressions for right angle case can be referred to from previous work [28] where C_1 and C_2 are functions of a as in Table 1.The geometry for this case, i.e., $\Delta Q_o P_{1,r} R_1$ and $\Delta Q_o P_{2,r} R_2$ can be constructed from the known results in Eq. (7). We can extend this specific case study to generate a general solution set using our geometry-based approach, as shown in Fig. 2b.

Any perturbations (scaling) along the line $\overline{P_{1,r}R_1}$ keeps the leg length ratio a constant. This implies that scaling of $\overline{P_{1,r}R_1}$ to generate $\overline{P_1R_1}$ (hence $\Delta Q_o P_1 R_1$) will keep design variables such as $R_{ti}(= R_{ti,r}), R_{to}(= R_{to,r})$ and $\theta_1 \backslash \theta_2 = \theta$ the same/common as in the right angle triangle case given in Eq. (7). To incorporate this scaling, another free/input scaling variable f is introduced, and the new height of MGSP in any general triangle ($\Delta Q_o P_1 R_1$) can be given as:

$$
H = fH_r = f\sqrt{\frac{Q(KC_1C_2 - a^2)}{KC_1^2}} \tag{8}
$$

This can be seen in Fig. 2b, where $\overline{P_1R_1} = f\;\overline{P_{1,r}R_1}$ and their lengths are directly proportional to H. The scaling variable f can be varied to generate different dynamic isotropic configurations with variable a constant. Each of the a values corresponds to a different triangle pair over which the variable f can vary depending on the expected design parameters' values for an MGSP. In each triangle pair, $f = 1$ corresponds to the right angle triangle case.

The new triangle pairs obtained due to scaling ($\Delta Q_o P_1 R_1$ and $\Delta Q_o P_2 R_2$) also satisfy all the isotropic/geometric conditions in Table 1 and represents a dynamically isotropic design. All other design variables for the general case

Table 2: General closed-form solution for design variables ($Y = 0$) in their explicit form

Variable	$R_{ti}(=\overline{Q_oR_1})$	$R_{to}(=\overline{Q_oR_2})$	$H\ (\propto \overline{P_1R_1}$ or $\propto \overline{P_2R_2})$
Solution	Same as Eq. (7)	Same as Eq. (7)	$=fH_r$ (see Eq. (8))
Variable	$R_{bi}(=\overline{Q_oP_1})$	$R_{bo}(=\overline{Q_oP_2})$	
Solution	See Eq. (9)	$\sqrt{\frac{QC_1}{a^2}+\frac{fQ(KC_1C_2-a^2)(2C_1+fC_2)}{KC_1^2a^2}}$	
Variable	$\tan(\alpha_{bi}-\alpha_{ti})\ (=\angle R_1Q_oP_1)$		$\tan\alpha_{to}\ (=\angle R_2Q_oP_2)$
Solution	$\left(\frac{fa\sqrt{(KC_1C_2\ -\ a^2)}}{KC_1C_2\ -\ f(KC_1C_2-a^2)}\right)$		$\left(\frac{b_2\ sin(\theta_2)}{R_{to}+\ b_2\ cos(\theta_2)}\right)$

$(R_{bo},\ \alpha_{to},\ R_{bi},\ \alpha_{bi}-\alpha_{ti})$ can be obtained in their explicit closed-forms by using geometrical relations in Fig. 2b and known variables in Eqs. (7) and (8). For, example,the variable R_{bi} can written as $\sqrt{(R_{ti}-b_1\cos\theta_1)^2+(b_1\sin\theta_1)^2}$ from the geometry in Fig. 2b, and we get

$$R_{bi}=\sqrt{\frac{QKC_1C_2+fQ(KC_1C_2-a^2)(f-2)}{KC_1}} \tag{9}$$

Similarly, using geometry, the unknown variables can be deduced from known variables, and the general solutions for each parameter are summarized in Table 2 in their explicit form. These solutions can be used for a straightforward design of a dynamically isotropic MGSP.

Observations.

3.1.1. Design parameter variation

The variation of design parameters of a dynamically isotropic MGSP with respect to free variables a and f will facilitate arriving at a suitable design respecting space and physical constraints. Figure 3 represents variation of parameters for a typical payload with $m_p = 10$ kg, $I_{xx} = 0.0663$ kg m^2, $I_{yy} = 0.0663$ kg m^2, and $I_{zz} = 0.1230$ kg m^2 for two values of f, i.e., 1 and 2.5. Any value of a in the case of $f = 1$ (refer to Figs. 3a and 3b) represents a right angle triangle ($\Delta Q_oP_{1,r}R_1$) in Fig. 2b. The height H of the platform is scaled up by 2.5 times when $f = 2.5$ (refer to Fig. 3c), in consistency with

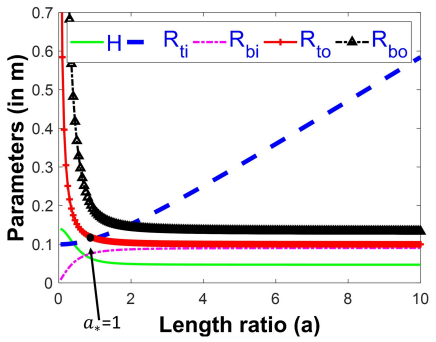

(a) For $f = 1$ (Right angle triangle solution set)

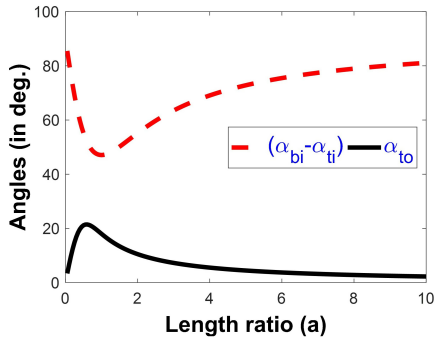

(b) For $f = 1$ (Right angle triangle solution set)

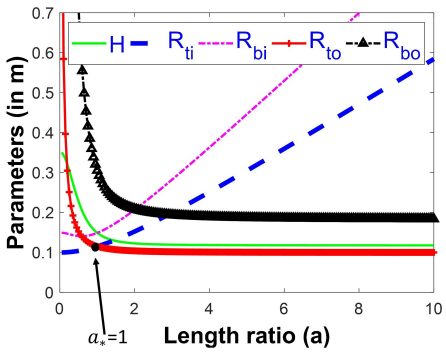

(c) For $f = 2.5$

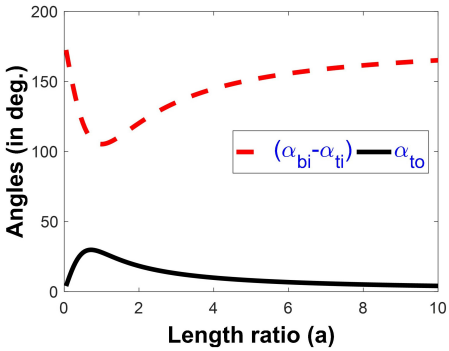

(d) For $f = 2.5$

Figure 3: Variation of parameters for a dynamically isotropic MGSP ($Y = 0$)

Eq. (8) (i.e. $H = fH_r$). It can also be observed that upon scaling (changing f), the variables $R_{ti}(= R_{ti,r})$ and $R_{to}(= R_{to,r})$ do not change – consistent with our geometry based approach, and can be observed in Fig. 2b.

Another interesting observation is that at $a = 1$, the two radii on the mobile platform become equal, i.e., $R_{to} = R_{ti}$ (irrespective of f). This is a point of configuration transition (a_*) where there is a transition of MGSP configuration from outer-outer (inner-inner) type leg connections ($a < 1$) to outer-inner (cross leg) type leg connections ($a > 1$) (see Figs. 3a and 3c). Outer-to-outer or inner-to-inner type leg connections imply that the outer radius of the mobile platform is connected to the outer radius of the base platform ($R_{to} > R_{ti}$ or $R_{bo} > R_{bi}$). In the case of $Y = 0$ (COM on the mobile platform), a_* is always equal to one, and the value of radius at this point is equal to $\sqrt{2Q}$ ($R_{ti} = R_{to} = \sqrt{2Q}$). All choices of MGSP design with $a < 1$

will ensure mechanical feasibility, as legs can never interfere in 3D space in these configurations. However, an investigation of feasibility is needed for design with $a > 1$.

3.1.2. Dynamically isotropic natural frequency

The design variables obtained in Table 2 can be substituted in Eqs. (4) and (6) to obtain equal first six natural frequencies given in terms of the mass of payload and axial stiffness of legs as:

$$\begin{aligned} \lambda_1 = \lambda_2 = \lambda_3 = \lambda_4 = \lambda_5 = \lambda_6 = \omega^2 \\ \text{and } \omega = \sqrt{2k/m_p} \end{aligned} \tag{10}$$

The total stiffness in all six legs, i.e., $6k$, will be uniformly distributed along the three independent axes in a dynamically isotropic MGSP ($2k$ in each direction) due to stiffness isotropy achieved along the translational directions and can be observed from Eq. (1). Hence, the dynamically isotropic natural frequency will be $\sqrt{2k/m_p}$, consistent with Eq. (10). This also implies that the absolute maximum of the lowest eigenfrequency is the same as dynamically isotropic natural frequency [19].

3.1.3. Invariant line with constant magnitude

There is an invariant line ($\overline{P_3R_3}$) in Fig. 2a whose length remains constant ($= \sqrt{2Q}$) irrespective of variable a (any triangle). However, the inclination of this line varies with a and is given as ϕ ($= \arctan(\sqrt{C_1/C_2})$).

3.1.4. Non-isotropy of Traditional GSP

The well-known fact that a traditional GSP does not have a dynamically isotropic configuration can also be verified by this geometry-based approach. To attain the necessary condition of $R_{bi} = R_{bo}$ and $R_{to} = R_{ti}$ for a traditional GSP, $\Delta Q_o P_1 R_1$ and $\Delta Q_o P_2 R_2$ in Fig. 2a must be congruent requiring angle θ_2 to be obtuse. This violated the dynamic isotropy condition in Table 2, i.e., $\tan\theta_1 = \tan\theta_2$.

3.2. COM not on the mobile platform ($Y \neq 0$)

In practice, the centre of mass (COM) of the MGSP is not on the mobile platform but varies with a payload mounted on the mobile platform. The insight gained from the case of Y=0 can now be extended to develop a general case considering the variation of the centre of mass. Simplifying the Eqs. (4),

(6) and Appendix, we can develop a similar geometry-based approach as in Section 3.1. The overall dynamic isotropy problem is reduced to a pair of triangles, but the value of each side now incorporates the variable Y, as seen in Fig. 4a. The major difference with respect to the previous case is that here $\theta_1 \neq \theta_2$ and similar to Section 3.1, a general triangle $\Delta Q_o P_1 R_1$ can be obtained by scaling side $\overline{P_{1,r}R_1}$ of right angle triangle $\Delta Q_o P_{1,r} R_1$ in Fig. 4b. Using Pythagoras theorem in $\Delta Q_o P_{1,r} R_1$ and solving all the conditions analytically in Eq. (6) (refer to [28] for detailed analytical development), we get all the variables for the right-angle triangle case as a function of payload properties and variable a given as:

$$
\begin{aligned}
H_r &= \sqrt{\frac{Q(KC_1C_2 - a^2)}{KC_1^2}} - Y = H_o - Y, \\
R_{ti,r} &= \sqrt{QC_2 + \ C_1Y^2 - \ 2YH_o\ C_1} \\
R_{bi,r} &= \sqrt{\frac{Qa^2}{KC_1}} \\
(\alpha_{bi,r} - \alpha_{ti,r}) &= \operatorname{atan}\left(\frac{C_1\sqrt{K}(-Y + H_o)}{a\sqrt{Q}}\right) \\
\theta_1 &= 90^\circ - (\alpha_{bi,r} - \alpha_{ti,r}) \\
R_{to,r} &= \sqrt{\frac{QC_1 + 2YH_o\ C_1 + C_2Y^2}{a^2}} \\
R_{bo,r} &= \sqrt{\frac{QC_1 + (2C_1 + C_2){H_o}^2}{a^2}} \\
\theta_2 &= \operatorname{acos}\left(\frac{R_{ti,r}\sqrt{C_1}\ \cos(\theta_1) + 2Y(a^2+1)}{aR_{to,r}\sqrt{C_2}}\right) \\
\alpha_{to,r} &= \operatorname{asin}\left(\frac{R_{bi,r}R_{ti,r}\sin(\alpha_{bi,r} - \alpha_{ti,r})}{a^2R_{bo,r}R_{to,r}}\right)
\end{aligned}
\tag{11}
$$

where $H_o = \sqrt{\frac{Q(KC_1C_2 - a^2)}{KC_1^2}}$ is a variable denoting the height of the platform in Eq. (8) (right angle triangle case for $Y = 0$ in the previous section). Interestingly, the height H_r (right-angle triangle case) in Fig. 4b is $H_o - Y$, and the total height from the base platform to COM will hence be H_o in both

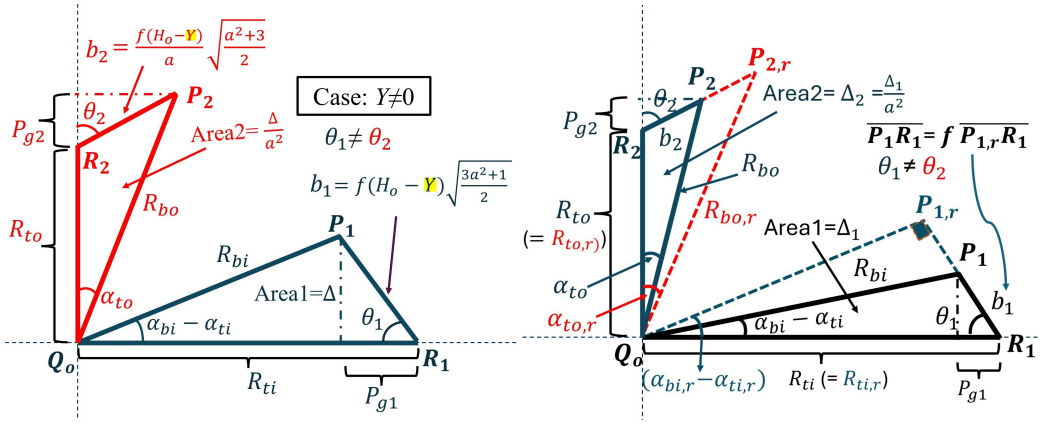

Figure 4: **a)** Geometrical interpretation of a dynamically isotropic MGSP ($Y \neq 0$) **b)** General triangle obtained using a corresponding right-angled triangle for $Y \neq 0$

the cases, i.e., when $Y = 0$ and $Y \neq 0$. For this reason, the dimension of the base platform variable ($R_{bo,r}$ and $R_{bi,r}$) supporting the same COM heights from the base is the same as in Eq. (7) and Eq. (11).

Similar to Section 3.1, $\Delta Q_o P_{1,r} R_1$ and $\Delta Q_o P_{2,r} R_2$ can be constructed from Eq. (11) and then scaling is done along the line $\overline{P_{1,r}R_1}$ to generate $\overline{P_1R_1}$ such that $\overline{P_1R_1} = f\ \overline{P_{1,r}R_1}$ (hence $\Delta Q_o P_1 R_1$ is generated). All other design variables for $Y \neq 0$ case apart from common variables (like $R_{ti}(= R_{ti,r})$, $R_{to}(= R_{to,r})$, θ_1, θ_2) can be derived using general trigonometry and geometry as:

$$
\begin{aligned}
H &= f(H_o - Y) \\
R_{bi} &= \sqrt{(R_{ti} - b_1 \cos\theta_1)^2 + (b_1 \sin\theta_1)^2} \\
R_{bo} &= \sqrt{(R_{to} + b_2 \cos\theta_2)^2 + (b_2 \sin\theta_2)^2} \\
\alpha_{bi} - \alpha_{ti} &= \arctan\left(\frac{b_1 \ \sin(\theta_1)}{R_{ti} - \ b_1 \cos(\theta_1)}\right) \\
\alpha_{to} &= \arctan\left(\frac{b_2 \ \sin(\theta_2)}{R_{to} + \ b_2 \cos(\theta_2)}\right)
\end{aligned}
\tag{12}
$$

where values of b_1 and b_2 are given in Table 1. Hence, all the desired dynamically isotropic design variables can be obtained from this approach with

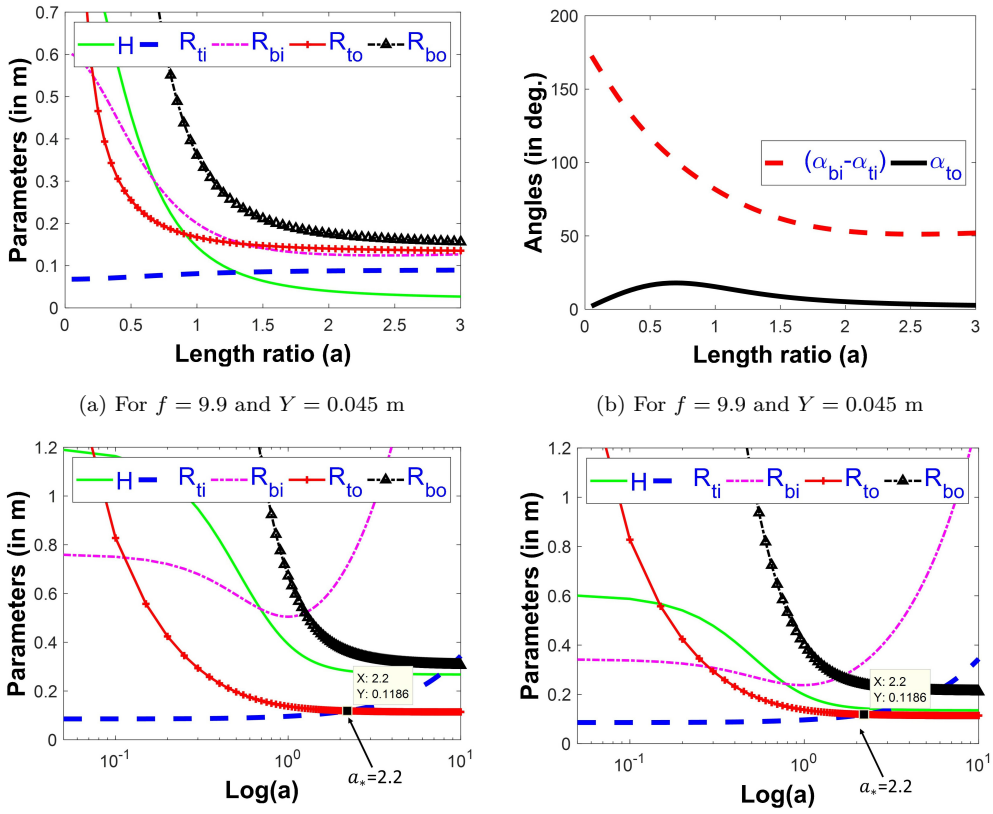

(a) For $f = 9.9$ and $Y = 0.045$ m

(b) For $f = 9.9$ and $Y = 0.045$ m

(c) For $f = 9.9$ and $Y = 0.02$ m

(d) For $f = 5$ and $Y = 0.02$ m

Figure 5: Variation of parameters for a dynamically isotropic MGSP with COM variation

input variables (a and f) and known payload variables Q, K, and Y.

Observations

The same set of observations as in the previous case can be seen when the COM is varied; However, COM variation (Y) affects the pattern of *variation of parameters*. Figures 5a and 5b show the parameters' variation of a dynamically isotropic MGSP for a typical payload of 10 kg (properties: $m_p = 10$ kg, $I_{xx} = 0.0663$ kg m^2, $I_{yy} = 0.0663$ kg m^2, and $I_{zz} = 0.1230$ kg m^2) with $Y = 45$ mm and $f = 9.9$. Here, no configuration transition point (a_* where $R_{to} = R_{ti}$) can be observed, implying only outer-outer (or inner-inner) type radius connections. The pattern of parameter variation changes when COM is changed from $Y = 45$ mm to $Y = 20$ mm in Fig. 5c. The point of config-

Table 3: DII in FE simulation for various cases

Case		Natural frequencies	DII
1	Analytically as in Section 3.2	30.46, 30.46, 30.46, 30.46, 30.46, 30.46	1.00
2	Conventional joint (section 4.1)	29.76, 30.26, 30.28, 30.57, 30.58, 30.60	1.028
3	Flexural joint in Fig. 6b	29.41, 29.46, 30.59, 30.06, 30.52, 30.55	1.039
4	Flexural joint in Fig. 6c	29.49, 29.51, 29.65, 30.17, 30.70, 30.71	1.041

uration transition (a_*) now occurs at point $a_* = a = 2.2$ and is in general, a function of variable Y. On the other hand, there is no change in a_* when variable f is varied to 5 in Fig. 5d. This is also evident from Fig. 4b, where variables R_{to} and R_{ti} remain the same on scaling $\overline{P_1R_1}$ (using variable f) for a given a. It is crucial to select the parameters with consideration of space constraints, particularly in spacecraft applications where space is extremely limited. The parameters $H+2Y$ and $\max(R_{bi}, R_{ti}, R_{bo}, R_{to})$ define the overall volume occupied by the setup.

Along similar lines, the dynamically isotropic natural frequency remains the same as in Eq. (10) ($\omega_1 = \omega_2 = ... = \omega_6 = \sqrt{2k/m_p}$)

4. Validation through simulation in ANSYS

Simulations were done on ANSYS® before arriving at the final design. The initial FEM considers using conventional joints and other assumptions (no damping) adopted during the analytical formulation. The FE model is later extended to flexural joints and including damping.

4.1. FEM validating analytical formulation

The mobile and base platforms are treated as rigid bodies and modeled using Shell 181 elements, while each leg is treated as an ideal spring (Link 180 element). The legs have no mass and inertia, while the payload is treated as a lumped mass. The multi-point constraint (MPC) beam was used to fix the payload (lumped mass) with the mobile platform. The leg stiffness

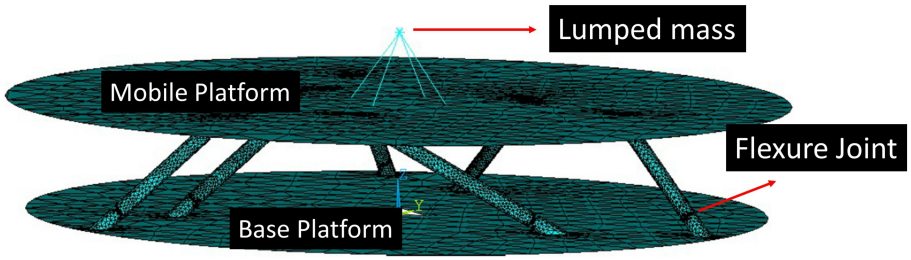

(a) Dynamically isotropic MGSP model in ANSYS

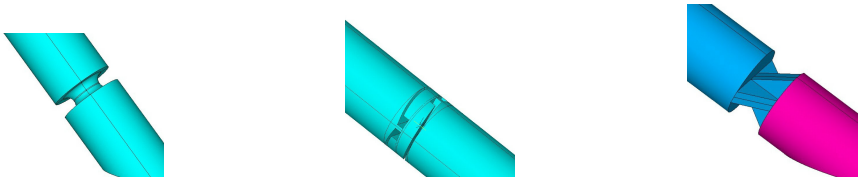

(b) (c) (d)

Figure 6: MGSP with various flexural joints

was chosen to be $k = 1.9 \times 10^5$ N/m without any damping to bear the launch loads. For a typical spacecraft wheel of 10 kg with properties listed in Section 3.2 and $Y = 45$ mm, a model was built satisfying all space constraints with variable $a = 1.4$ and $f = 9.9$ giving height $H = 73$ mm. The joints resemble conventional joints as in the analytical formulation, and all the parameters for FEM are taken using the geometry-based approach discussed in the previous section. All six natural frequencies were found very close to each other, validating analytical formulation (refer to Case 2 in Table 3) with DII=1.028. Dynamic isotropy index (DII) quantifies the frequency spread, representing the ratio of the largest to the smallest natural frequency among the first six modes. Our results in all configurations are very close to the ideal dynamically isotropic MGSP with the same natural frequencies (DII=1, refer to Case 1, Table 3). The natural frequencies obtained are very close to analytical natural frequency ($\omega_1 = \omega_2 = ... = \omega_6 = \sqrt{2k/m_p}$).

4.2. FE Analysis with flexural joints based MGSP considering damping

The use of conventional joints for the application of vibration isolation in spacecraft can induce backlash error, friction, and lubrication issues. Therefore, using flexural joints instead of conventional joints in MGSP is a viable solution for this application at the expense of additional parasitic stiffness,

as shown in Fig. 6a. Ideally, a flexural joint for this application should have low bending stiffness, high axial stiffness, high shear stiffness, and low torsional stiffness [5, 7, 9]. High axial stiffness ensures passing on the control load to the mobile platform in an active vibration isolation system. This also ensures the safe distribution of the launch loads across the legs. The local modes of the legs should occur at higher frequencies, demanding a higher shear stiffness flexural joint design to avoid interference in the working range of the MGSP (i.e., the required isolation region). The spread of the natural frequency can be minimized to a narrow bandwidth with low bending and torsional stiffness design. Various flexural joints depicted in Figs. 6b, 6c and 6d in a dynamically isotropic MGSP design were explored along these lines, and the results listed in Cases 3 and 4 in Table 3 confirms its effectiveness for use in vibration isolation applications. The inclusion of bending stiffness due to flexural joints, $[\mathbf{K}_b]$, in the analytical model [5] alters the overall stiffness matrix in Eq. (1) as follows:

$$[\mathbf{K}_T] = k[\mathbf{B}][\mathbf{B}]^T + [\mathbf{K}_b] \tag{13}$$

Nonetheless, the influence of the $[\mathbf{K}_b]$ term is minimal, as indicated by the negligible difference in the DII values between conventional joints and flexural joints in Table 3. Therefore, it is reasonable to disregard the bending stiffness effect for the flexural joints in the analytical formulations employed in this study. All the parts are made of Aluminum alloy 2024 and possess an inherent structural damping. Hence, the leg assemblies are given equivalent viscous damping of around $\zeta = 2$ % (in their joint space) within the standard range, being treated as continuous metal structures with flexural joints. The damping model is incorporated in our analytical formulations in Section 6.2 after the study of experimental damping values.

4.2.1. Frequency Response Function (FRF) of the MGSP

The FRF of the dynamically isotropic MGSP can be seen in Fig. 7a where the three modes (i.e., $\boldsymbol{X}$, $\boldsymbol{Y}$ and $\boldsymbol{Z}$) are observed to overlap each other perfectly. The steady-state dynamics of the MGSP were studied by exciting the base with unit displacement in all DOFs (rotations and translations one by one), respectively. The FRF curves define the relations between the response of COM of the payload and inputs given to the base platform. The overlapping of curves indicates that the damping is uniformly distributed across the three axes, and their values are calculated using the half-power bandwidth

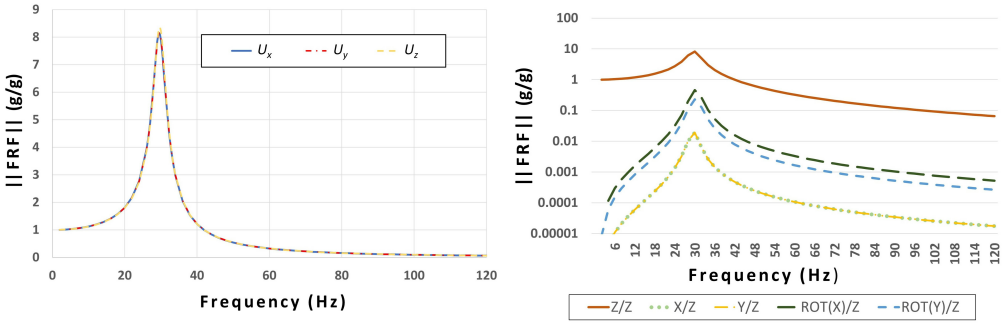

(a) FRF of the $\boldsymbol{X}$, $\boldsymbol{Y}$ and $\boldsymbol{Z}$ modes

(b) FRF : when only $\boldsymbol{Z}$ mode is excited

Figure 7: FEM results

method as listed in Table 5. FEM results indicate that MGSP will have an overall equivalent viscous damping of nearly 4% in all the modes. The comparison with the experimental and analytical results will later be discussed in Section 6. Another important observation from this analysis was the minimal or negligible interference of the cross-DOF modes when a particular DOF mode is excited. For e.g., Fig. 7b shows FRF in the log scale when the translational mode along the $\boldsymbol{Z}$ is excited and all cross-mode responses are seen to have relatively negligible value, which is a required characteristic for our application.

4.2.2. Mode shapes of the MGSP

The MGSP mode shapes show pure bending, bounce, and torsion mode with a small amount of mixing of other modes, as shown in Fig. 8, while shear dominant mode exists with a mixture of bending modes. The first two modes are shear dominant bending type and similar in nature along the perpendicular axis $\boldsymbol{X}$ and $\boldsymbol{Y}$ (refer to Fig. 8a). The center of the mobile platform has significant displacement in the shear case, contrary to the pure bending case in Fig. 8d, where it has negligible displacement at the center. The last two modes are pure bending modes (refer to Fig. 8d) about $\boldsymbol{X}$ and $\boldsymbol{Y}$ axis. The third and fourth modes are pure bounce and torsion mode, as evident from Fig. 8b and 8c.

4.2.3. Final model and prototype

The CAD model, as shown in Fig. 9a, was finalized after considering all the constraints and gaining experience from the development process of

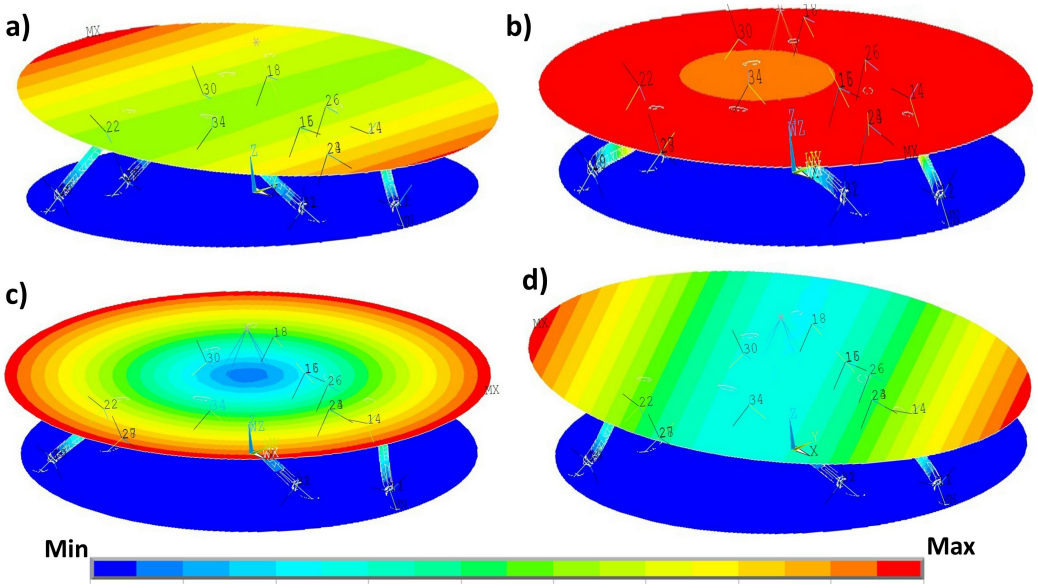

Figure 8: **a)** Shear dominant plus bending mode (first two) **b)** Bounce/Plunge mode **c)** Torsion mode **d)** Bending mode (last two modes)

MGSP design. The mobile platform, along with fixed boundary conditions at the anchorage points, has a sufficiently high natural frequency (order of $\sim$ 700 Hz), preventing its interference in the isolation region. The triangle shape of the mobile platform is designed to save mass; however, it does affect the overall asymmetricity property of the payload (mobile platform plus wheel). A dummy wheel, as shown in Fig. 9b with approximately similar inertia properties to the 10 kg reaction wheel (refer to Section 3.2), was used for testing purposes.

5. Experimental Setup

The actual MGSP prototype, as shown in Fig. 10, was fabricated and tested with the dummy wheel payload at the ISRO vibration test facility. The flexural joints shown in Fig. 10a were realized through the electrical discharge machining method. All six modes of MGSP (rotational and translational) were extracted using different methods.

The lateral modes ($\boldsymbol{X}$ and $\boldsymbol{Y}$ modes) were obtained by mounting the fixed base on the slip table as shown in Fig. 10a and exciting the base platform with an acceleration sine sweep of 0.5 g constant amplitude sweeping from 5-

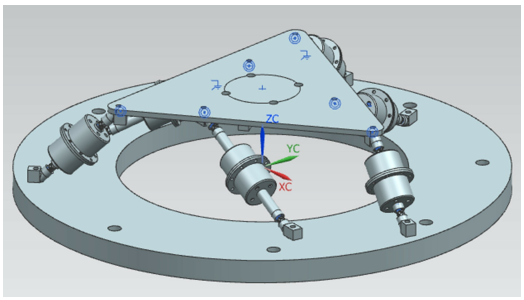

(a) Final dynamically isotropic MGSP CAD model

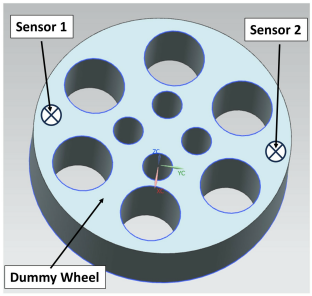

(b) Dummy payload wheel

Figure 9: Final Design

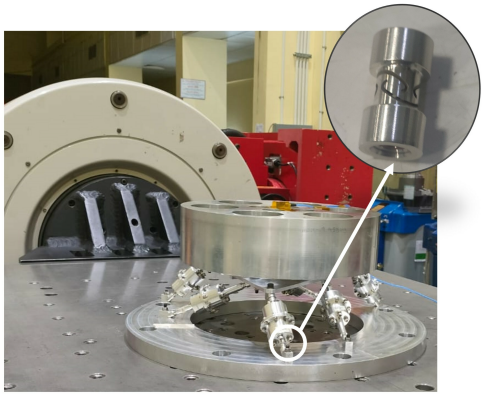

(a) Slip table for $\boldsymbol{X}$ and $\boldsymbol{Y}$ modes

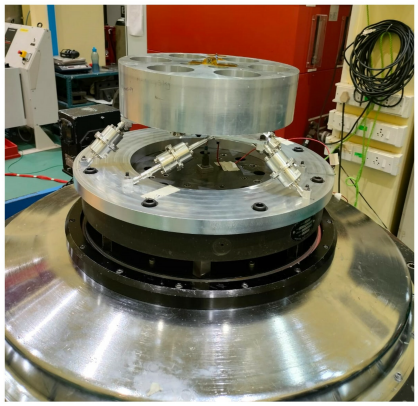

(b) Longitudinal electro-dynamic shaker for $\boldsymbol{Z}$ mode

Figure 10: Dynamically isotropic MGSP Prototype with test setups

500 Hz. The response was captured using tri-axial accelerometers (Make: B & K, Model: 4517-002, sensitivity: approximately 10 mV/g) mounted on the center of the payload wheel and fixed platform. The acceleration data were acquired at 1 kHz, and the corner frequencies of the MGSP were extracted from the FRF data. The longitudinal $\boldsymbol{Z}$ mode was obtained by mounting the platform on a 4-ton rating electro-dynamic shaker (Make: Ling Dynamic System, LDS, Model: 953 VIBRATOR TC.MPS 32) with the same excitation signal used for the lateral modal test (refer to Fig. 10b). The total payload mass (wheel and the mobile platform) was 10.37 kg, while the stiffness of the legs was the same as $k = 1.9 \times 10^5 N/m$.

The rotational modes were obtained using the impact hammer test, where two accelerometers were mounted on the diametrically opposite ends of the

Table 4: Comparison of natural frequencies of MGSP obtained via analytical solution, FEM, and Experiment in Hz

Modes	***X***	***Y***	***Z***	Rot ***X***	Rot ***Y***	Rot ***Z***
Analytical	30.46	30.46	30.46	30.46	30.46	30.46
FEM	29.49	29.51	29.65	30.70	30.71	30.17
Experiment	28.75	29.00	29.25	29.49	29.58	29.10

Table 5: Comparison of damping (in %) in MGSP obtained via FEM and Experiment

Modes	***X***	***Y***	***Z***	Rot ***X***	Rot ***Y***	Rot ***Z***
FEM	4.23	4.23	4.00	3.30	3.60	3.50
Experiment	$\sim$ 5.90	$\sim$ 4.90	$\sim$ 6.30	$\sim$ 3.41	$\sim$ 3.43	$\sim$3.05

payload, similar to Fig. 9b. The time domain data were acquired for each axis using the combination of data from these two sensors. Therefore, the damping for rotational modes was calculated using the logarithmic decrement method (time domain), while the damping for translation mode was calculated using the half-power bandwidth method (frequency domain).

6. Results and discussion

The analytical, FEM, and experimental results for natural frequency and damping are shown in Tables 4 and 5. It can be concluded that the natural frequencies for all the modes are close to FE and analytical method results. The damping related to the Quality factor of the FRF curve is almost equal in all three translation modes, similar to the FE result discussed in Section 4.2.1. The damping results for rotational modes obtained via time domain data also closely resemble each other in Table 5. The FRF curves for ***X***, ***Y*** and ***Z*** modes obtained experimentally can be seen in Fig. 11a, and the comparison of the curves with FE results for each axis can be seen in Figs. 11b, 11c and 11d. The equivalence of vital parameters like damping and natural frequencies was confirmed through these curves, even though peak amplitude differs slightly between the experiment and the FE simulation. The difference in peak can be justified as the exact value of damping is difficult to predict in the assemblies. Additionally, the MGSP base was mounted to the test setup via bolted joints during experimentation, while the inputs were directly given to the base plate in case of FE analysis. The friction at the joints in the prototype was not taken into account in the computations. The roll-off after resonance for ***X***,

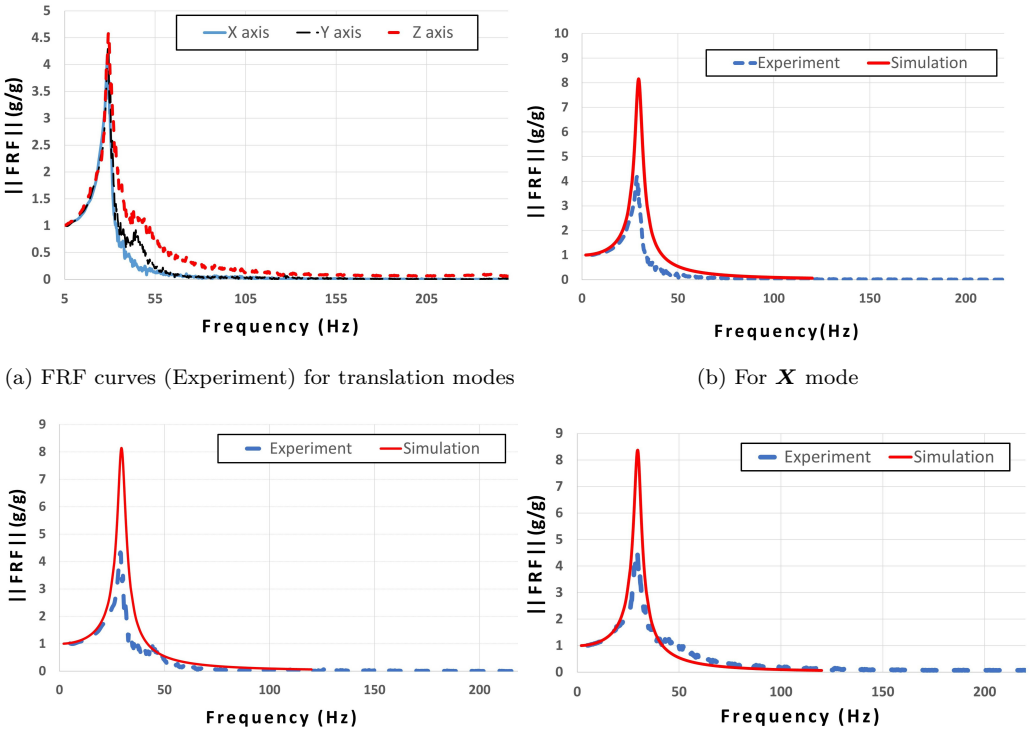

(a) FRF curves (Experiment) for translation modes

(b) For $\boldsymbol{X}$ mode

(c) For $\boldsymbol{Y}$ mode

(d) For $\boldsymbol{Z}$ mode

Figure 11: Experimental result for translation modes (i.e, $\boldsymbol{X}$, $\boldsymbol{Y}$ and $\boldsymbol{Z}$ modes)

$\boldsymbol{Y}$, and $\boldsymbol{Z}$ modes is approximately 29 dB/octave, both in simulation and experimental results. Furthermore, the slopes in the region of isolation are approximately 17-22 dB/octave (after the corner frequencies).

The performance of our isolators is superior or comparable in all aspects to the well-known isolator developed at ULB, based on cubic GSP and voice coil actuation [7]. From the transmissibility curve in [7], it is observed that the slope in the isolation region without control is 14 dB/octave, and the slope after incorporating active control is around 12 dB/octave. The peak is reduced from about 23 dB (without control) to about 5 dB/octave (with active control) in this work. Hence, our dynamically isotropic MGSP as a passive isolator performs well while also saving mass, power, and computational resources compared to the active control cubic GSP. Ideally, there should be no overshoot in active vibration isolation, but an overshoot of around 5 dB is observed in [7] due to the relatively high frequency spread with a DII of

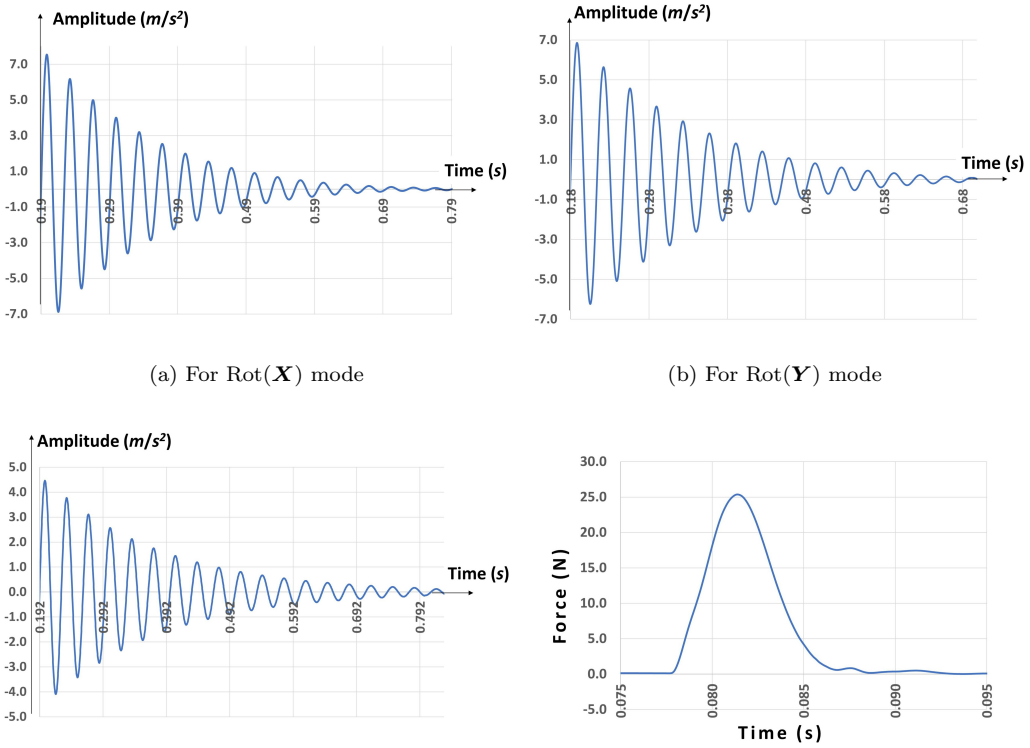

(a) For Rot($\boldsymbol{X}$) mode

(b) For Rot($\boldsymbol{Y}$) mode

(c) For Rot($\boldsymbol{Z}$) mode

(d) Impact hammer force data

Figure 12: Experimental result for Rotational modes (one data set of impact hammer test)

2.2, reflecting its non-dynamic isotropic design. This overshoot is also comparable to our passive dynamically isotropic MGSP, demonstrating that our isolator performs reasonably well in the low-frequency amplification region despite being passive-based. In the future, incorporating active damping with a dynamically isotropic configuration in our work can further reduce the overshoot to around the ideal case of 0 dB (transmissibility of one) in the amplification region. Therefore, our dynamically isotropic-based isolator performs well in both the amplification and isolation regions compared to existing GSPs, highlighting the value of achieving dynamic isotropy.

A similar observation can be seen for rotational mode in Tables 4 with natural frequencies equal to each other and also to the three translational modes. Damping in rotational modes (refer to Table 5) can be seen as equal to each other and quite close to the translational modes. Hence, it can be concluded that dynamic isotropic configuration distributes damping uniformly

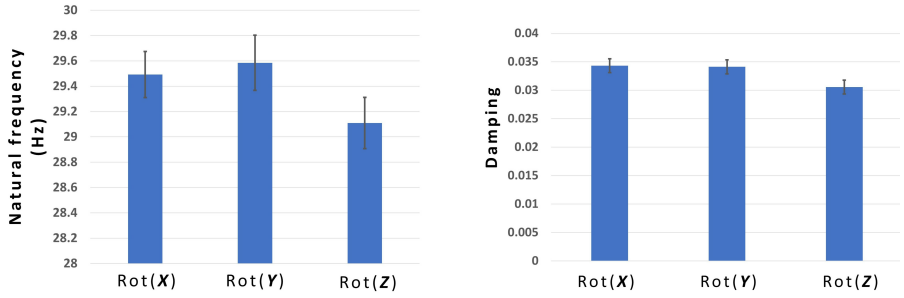

(a) Standard deviation for natural frequency

(b) Standard deviation for damping

Figure 13: Result for Rotational modes (Five experiment sets)

in rotational modes (like in translational modes), given identical damping in leg assemblies. The time domain data (from accelerometers) used for calculating natural frequency and damping parameters for Rot($\boldsymbol{X}$), Rot($\boldsymbol{Y}$), and Rot($\boldsymbol{Z}$) is shown in Fig. 12. The two accelerometer's data for Rot($\boldsymbol{X}$) and Rot($\boldsymbol{Y}$) DOFs have an opposite phase owing to their diametrically opposite placements, and their difference would reflect the rotational parameters. Five hammer tests were repeated for each rotation DOFs, and the standard deviations from the mean results are depicted in Figs. 13a and 13b.

6.1. Analytical vs. FEM vs. Experimental Results

All forms of results for a dynamically isotropic MGSP have a close resemblance with minor discrepancies of approximately 0.5-1 Hz for natural frequency and about 0.01 for damping. Such discrepancies arise primarily due to various factors and underlying assumptions. Firstly, our analytical formulations assume that the legs possess negligible mass and inertia, contrary to the prototype. However, these values are very small compared to the actual mass of a 10.37 Kg payload (each leg is around 110-120 grams[1]). The legs in the analytical formulation assume only axial stiffness in contrast with real-world scenarios where bending and other stiffness come into play with flexural joints instead of conventional joints. The FE and the prototype have damping, which slightly influences the resonance peak obtained with respect to the case with no damping in the analytical formulation. Another important factor to be considered is the slight deviation in the mass

[1]Smaller legs are 110 grams with a radius of gyration 23.58 mm while longer legs are 120 grams with a radius of gyration of 33.02 mm

and inertia properties of the payload (dummy mass and mobile platform). The payload was assumed to be asymmetric, but incorporating a triangular platform along with a dummy wheel slightly disrupts the symmetrical distribution of the properties along $\boldsymbol{X}$ and $\boldsymbol{Y}$ axis. For the same reason, the mass/inertia matrix is not diagonal but it is still diagonal dominant. Practical challenges further affect precision – achieving the intended stiffness of the legs ($k = 1.9 \times 10^5 N/m$) with high accuracy is difficult to obtain due to small material property variations. The error induced during the fast fourier transform (FFT) overestimates the experimental damping for $\boldsymbol{X}$, $\boldsymbol{Y}$ and $\boldsymbol{Z}$ modes. Moreover, the FRF curve exhibits dynamic changes around the resonance frequency, and using a step size of 0.25 Hz for translational modes will capture the properties only at intervals of 0.25 Hz. Determining exact structural damping in legs with different lengths seems tedious, leading to inevitable differences between practical and FEM results, especially when assuming equal structural damping for all legs.

Despite these complexities, the final outcomes are promising, demonstrating uniform natural frequencies of approximately 29 Hz and effective isolation beginning around 41 Hz. This isolator can be used to effectively isolate vibration from the spacecraft bus, offering substantial reductions in amplitude at the mobile platform of the MGSP. For instance, reductions of up to 23.60 dB, 21.28 dB, and 17.30 dB in $\boldsymbol{X}$, $\boldsymbol{Y}$, and $\boldsymbol{Z}$ axis, respectively, can be achieved from the vibration resulting for a typical reaction wheel operating at an average RPM of 4200 Hz.

6.2. Incorporating damping in the analytical formulation

As previously discussed, accurately predicting damping in the theoretical model is challenging and can be determined experimentally. By obtaining the damping through experimental methods, we can develop the most appropriate model for damping. The dynamic equation for MGSP [9] in the case of free vibration is given by:

$$\ddot{\boldsymbol{X}} + [\mathbf{M}]^{-1}[\mathbf{C}_T]\ \dot{\boldsymbol{X}} + [\mathbf{M}]^{-1}[\mathbf{K}_T]\ \boldsymbol{X} = 0 \tag{14}$$

where $\mathbf{X} = [X; Y; Z; \mathrm{Rot}(X); \mathrm{Rot}(Y); \mathrm{Rot}(Z)]$. Similar to Eq. (1), the damping matrix $[\mathbf{C}_T]$ can be written in the task space as $c[\mathbf{B}][\mathbf{B}]^T$ with c being the damping constant along each leg. For a linear hysteretic material subjected primarily to uniaxial loading, the loss factor(η) remains independent of the stress field and can be considered a material constant. For such a material,

we can construct a single degree of freedom (Kelvin-Voigt model) with equivalent viscous damping along each leg [29]. With excitation frequency as ω_e, the equivalent damping constant c can be given as:

$$c = \frac{k\eta}{\omega_e} \tag{15}$$

In a dynamically isotropic design, Eq. (14) reduces to six identical single DOF equations of the form:

$$\ddot{x} + \frac{\eta}{\omega_e}\omega^2 \, \dot{x} + \omega^2 \, x = 0 \tag{16}$$

and a dynamically isotropic system uniformly distributes damping. At the resonant frequency, the loss factor η_o and equivalent viscous damping of the system ζ_o are related to the loss factor η in a single DOF leg subjected to uniaxial load as:

$$\zeta_o = \frac{\eta_o}{2} = \frac{\eta}{2} \tag{17}$$

The theoretical FRF curve can be derived from Eq. (16), and its comparison with FE and experimental results for $\boldsymbol{Z}$ translation mode FRFs is shown in Fig. 14a. An approximate 2% damping is observed in the system using the theoretical model with the highest peak at resonance – the amplitude of the peaks from the FE model and experiments are smaller. This is because the theoretical model assumes the legs are subjected only to uniaxial loads and have conventional joints, while in the FE model with rigid connections, other types of loads at the flexural joints in the legs are present. Additionally, the FE model does not account for damping due to friction in the joints. The experimental FRF shows the lowest peak among all, as it includes additional frictional damping in all the components of the system. The FE and theoretical FRF curves overlap in the isolation region due to the dominance of excitation frequency over the small values of the loss factor, while the experimental curve (with nearly the same slope) is offset due to the dependence of material properties on the stress field and excitation frequency in the actual material, which is challenging to account in theoretical and FEM modeling.

A practical approach to address the assumption of considering only uniaxial loading is to assign the leg assemblies in the theoretical model with the same damping obtained from FE or experimental data. When equivalent damping of 4% from the FE model is applied to the leg assembly in the

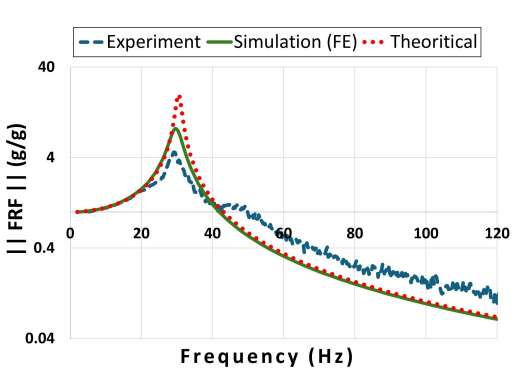

(a) 2 % damping in the leg assemblies

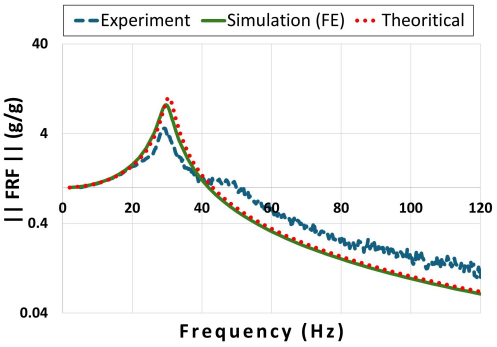

(b) 4 % damping in the leg assemblies (value from FE model)

Figure 14: FRF curve for $\boldsymbol{Z}$ mode including damping in the analytical formulation

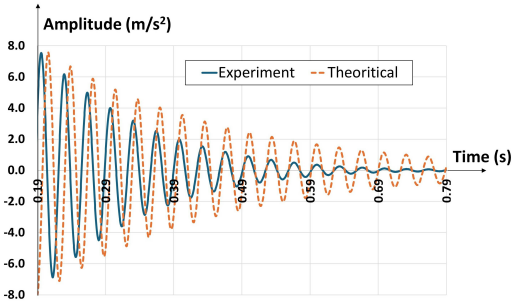

(a) 2 % damping in the leg assemblies

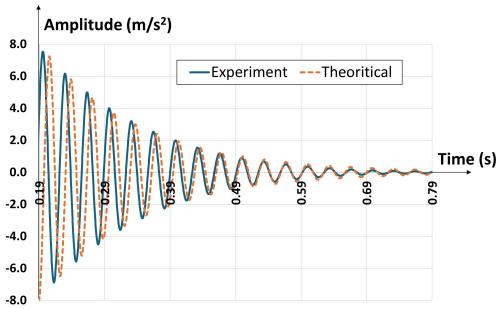

(b) 3.4 % damping in the leg assemblies(value from experiment)

Figure 15: Comparison of dynamic response for Rot($\boldsymbol{X}$) mode by including damping in the analytical formulation

analytical model, the FRF curves obtained using analytical results and FE closely match and can be seen in Fig. 14b. This validates the incorporation of damping in our analytical model.

Similarly, for Rot($\boldsymbol{X}$) mode depicted in Fig. 15a, the amplitudes of the dynamic responses exhibit variation when 2% damping is assigned to the leg assemblies, which does not account for frictional damping or addresses the challenge of uniaxial loading. However, when a damping of 3.4 % obtained experimentally is applied to Eq. (16) at their resonant frequency, the dynamic responses obtained using the analytical approach and experiment show close resemblance, as observed in Fig. 15b. This validates our analytical approach for accounting damping in our system.

7. Conclusion

This work presents the development process of a dynamically isotropic Modified Gough Stewart platform (MGSP) in detail. A novel geometry-based approach, based on a pair of triangles, is used to derive the various design parameters for a dynamically isotropic design with equal first six natural frequencies corresponding to the first six degrees of freedom. The multiple solutions offer flexibility in design, aiding in the selection of designs satisfying space constraints and other feasibility challenges. Simulations were done in ANSYS® with the selected design for our intended application of micro-vibration isolation. The MGSP design incorporating flexural joints was explored to overcome the friction, lubrication, and backlash issues of conventional joints. Damping was incorporated into the FE model and later in the analytical formulation. A prototype of a dynamically isotropic MGSP with flexural joints was built, and experiments revealed encouraging results for its application in micro-vibration isolation in spacecraft. The study's findings, including the convergence of analytical, FEM, and experimental results, provide compelling support for this conclusion. The first six natural frequencies in all the cases were nearly the same (around 29 Hz), and the damping was found to be close in rotational and translational modes. The region of isolation begins around 41 Hz for our applications, providing isolation of about 22 dB/octave. Using the general design methodology presented, a dynamically isotropic MGSP can be designed for a payload in an application requiring vibration isolation. Our findings demonstrate that our dynamically isotropic-based isolator performs effectively in both amplification and isolation regions compared to existing isolators.

In the future, we plan to explore integrating control mechanisms into our analytical model. An active vibration control system is known to achieve minimal amplification at resonance while facilitating substantial attenuation in the high-frequency spectrum (the region of isolation). Active vibration entails a mass penalty due to the inclusion of electronic and other components and incurs power consumption, a critical consideration in many space applications. These and other aspects of vibration isolation will be taken up in the future.

Acknowledgments

The authors are immensely grateful for the unwavering support received from the scientists and personnel of the Indian Space Research Organization

during the design and experimentation process.

Appendix

For Section (3), the value of all λs and μs in Eq. (4) are given as:

$$\lambda_1 = \frac{3k\ \left(l_{o1}^2\Psi_1 + l_{o2}^2\Psi_2\right)}{(2m_p l_{o1}^2 l_{o2}^2)},\ \lambda_2 = \frac{3k\ \left(l_{o1}^2\Psi_1 + l_{o2}^2\Psi_2\right)}{(2m_p l_{o1}^2 l_{o2}^2)},$$

$$\lambda_3 = \frac{3kH^2\left(l_{o1}^2 + \ l_{o2}^2\right)}{(m_p l_{o1}^2 l_{o2}^2)},$$

$$\lambda_4 = \frac{3kY^2\left(\ l_{o2}^2\Psi_2 + l_{o1}^2\Psi_1\right) + 6HkY\left(\Psi_3 l_{o1}^2 + \Psi_4 l_{o2}^2\right)\ +\ 3k\Psi_5 H^2}{(2I_{xx} l_{o1}^2 l_{o2}^2)},\quad \lambda_5 = \lambda_4\frac{(I_{xx})}{(I_{yy})},$$

$$\lambda_6 = \frac{3k\left(\Psi_6^2 l_{o1}^2 + \ \Psi_7^2 l_{o2}^2\right)}{(I_{zz} l_{o1}^2 l_{o2}^2)},$$

$$\mu_{11} = \frac{-3kH\left(-\Psi_6 l_{o1}^2 + \ \Psi_7 l_{o2}^2\right)}{(2l_{o1}^2 l_{o2}^2)},\ \mu_{33} = \frac{3kH\left(-\Psi_6 l_{o1}^2 + \ \Psi_7 l_{o2}^2\right)}{(l_{o1}^2 l_{o2}^2)},$$

$$\mu_{12} = \frac{3kH\left(\Psi_3 l_{o1}^2 + \Psi_4 l_{o2}^2\right) + 3kY\left(l_{o1}^2\Psi_1 + l_{o2}^2\Psi_2\right)}{(2l_{o1}^2 l_{o2}^2)}$$

where,

$$\Psi_1 = R_{ti}^2 + \ R_{bi}^2 - 2R_{ti}R_{bi}\cos\left(\alpha_{bi} - \alpha_{ti}\right)$$

$$\Psi_2 = R_{to}^2 + \ R_{bo}^2 - 2R_{to}R_{bo}\cos\left(\alpha_{to}\right)$$

$$\Psi_3 = R_{ti}^2 - R_{ti}R_{bi}\cos\left(\alpha_{bi} - \alpha_{ti}\right)$$

$$\Psi_4 = R_{to}^2 - R_{to}R_{bo}\cos\left(\alpha_{to}\right)$$

$$\Psi_5 = R_{ti}^2 l_{o1}^2 + \ R_{to}^2 l_{o2}^2$$

$$\Psi_6 = R_{ti}R_{bi}\sin\left(\alpha_{bi} - \alpha_{ti}\right)$$

$$\Psi_7 = R_{to}R_{bo}\sin\left(\alpha_{to}\right)$$

$$l_{o1} = \left(\sqrt{R_{to}^2 + R_{bo}^2 - 2R_{to}R_{bo}\cos\left(\alpha_{to}\right) + H^2}\right)$$

$$l_{o2} = \left(\sqrt{R_{ti}^2 + R_{bi}^2 - 2R_{ti}R_{bi}\cos\left(\alpha_{bi} - \alpha_{ti}\right) + H^2} \right)$$

References

[1] N. Ahmad, Vibration mitigation in spacecraft components using Stewart platform and particle impact damping, PhD Thesis, Indian Institute of Science (2020).

[2] L. Li, L. Tan, L. Kong, D. Wang, H. Yang, The influence of flywheel micro vibration on space camera and vibration suppression, Mechanical Systems and Signal Processing 100 (2018) 360–370. doi:10.1016/j.ymssp.2017.07.029.

[3] J.-M. L. Duigou, Microvibration measurements on Spot 4, results of the micromedy Experiment, Spacecraft Structures, Materials and Mechanical Testing 428 (1999) 475–483.

[4] G. Aglietti, G. Kerschen, J. Albus, W. Konrad, M. Bellini, ECSS, Space engineering; Spacecraft mechanical loads analysis handbook, Noordwijk, ECSS-E-HB-32-26A (February 2013).

[5] A. A. Hanieh, Active isolation and damping of vibrations via Stewart platform, PhD Thesis, ULB ASL (2003).

[6] C. Wang, X. Xie, Y. Chen, Z. Zhang, Investigation on active vibration isolation of a Stewart platform with piezoelectric actuators, Journal of Sound and Vibration 383 (2016) 1–19. doi:https://doi.org/10.1016/j.jsv.2016.07.021.

[7] A. Preumont, M. Horodinca, I. Romanescu, B. de Marneffe, M. Avraam, A. Deraemaeker, F. Bossens, A. Abu Hanieh, A six-axis single-stage active vibration isolator based on Stewart platform, Journal of Sound and Vibration 300 (3) (2007) 644–661. doi:https://doi.org/10.1016/j.jsv.2006.07.050.

[8] R. B. A. Shyam, N. Ahmad, R. Ranganath, A. Ghosal, Design of a dynamically isotropic Stewart-Gough platform for passive micro-vibration isolation in spacecraft using optimization, Journal of Spacecraft Technology 30 (2) (2019) 1–8.

[9] H. Yun, L. Liu, Q. Li, W. Li, L. Tang, Development of an isotropic Stewart platform for telescope secondary mirror, Mechanical Systems and Signal Processing 127 (2019) 328–344. doi:https://doi.org/10.1016/j.ymssp.2019.03.001.

[10] Y. Yi, J. E. McInroy, F. Jafari, Generating classes of locally orthogonal Gough-Stewart platforms, IEEE Transactions on Robotics 21 (5) (2005) 812–820. doi:10.1109/TRO.2005.851360.

[11] J. McInroy, F. Jafari, Finding symmetric orthogonal gough-stewart platforms, IEEE Transactions on Robotics 22 (5) (2006) 880–889. doi:10.1109/tro.2006.878975.

[12] A. Fattah, A. M. H. Ghasemi, Isotropic design of spatial parallel manipulators, The International Journal of Robotics Research 21(9) (2002) 811–824. doi:https://doi.org/10.1177/027836490202100984 2.

[13] S. Bandyopadhyay, A. Ghosal, An algebraic formulation of kinematic isotropy and design of isotropic 6-6 stewart platform manipulators, Mechanism and Machine Theory 43 (5) (2008) 591–616. doi:10.1016/j.mechmachtheory.2007.05.003.

[14] J. Zhenlin, G. Feng, Z. Xiaohui, Design and analysis of a novel isotropic six-component force/torque sensor, Sensors and Actuators A: Physical 109 (1–2) (2003) 17–20. doi:10.1016/s0924-4247(03)00299-1.

[15] S. Bandyopadhyay, A. Ghosal, An algebraic formulation of static isotropy and design of statically isotropic 6–6 Stewart platform manipulators, Mechanism and Machine Theory 44 (7) (2009) 1360–1370. doi:10.1016/j.mechmachtheory.2008.11.002.

[16] J. Yao, Y. Hou, H. Wang, T. Zhou, Y. Zhao, Spatially isotropic configuration of Stewart platform-based force sensor, Mechanism and Machine Theory 46 (2) (2011) 142–155. doi:10.1016/j.mechmachtheory.2010.10.002.

[17] Z. Chong, F. Xie, X.-J. Liu, J. Wang, Evaluation of dynamic isotropy and coupling acceleration capacity for a parallel manipulator with mixed dofs, Mechanism and Machine Theory 163 (2021) 104382. doi:10.1016/j.mechmachtheory.2021.104382.

[18] H.-Z. Jiang, Z.-Z. Tong, J. feng He, Dynamic isotropic design of a class of Gough-Stewart parallel manipulators lying on a circular hyperboloid of one sheet, Mechanism and Machine Theory 46 (3) (2011) 358–374. doi:10.1016/j.mechmachtheory.2010.10.008.

[19] B. Afzali-Far, P. Lidström, Analytical index of dynamic isotropy and its application to hexapods, Precision Engineering 52 (2018) 242–248. doi:http://dx.doi.org/10.1016/j.precisioneng.2018.01.001.

[20] B. Afzali-Far, P. Lidström, A Class of Generalized Gough-Stewart Platforms Used for Effectively Obtaining Dynamic Isotropy – An Analytical Study, MATEC Web of Conferences 35 (2015) 02002:P.1–P.5. doi:https://doi.org/10.1051/matecconf/20153502002.

[21] X. Yang, H. Wu, Y. Li, B. Chen, Dynamic isotropic design and decentralized active control of a six-axis vibration isolator via stewart platform, Mechanism and Machine Theory 117 (2017) 244–252. doi:10.1016/j.mechmachtheory.2017.07.017.

[22] Y. Wu, K. Yu, J. Jiao, D. Cao, W. Chi, J. Tang, Dynamic isotropy design and analysis of a six-dof active micro-vibration isolation manipulator on satellites, Robotics and Computer-Integrated Manufacturing 49 (2018) 408–425. doi:10.1016/j.rcim.2017.08.003.

[23] P. Mukherjee, B. Dasgupta, A. Mallik, Dynamic stability index and vibration analysis of a flexible Stewart platform, Journal of Sound and Vibration 307 (3–5) (2007) 495–512. doi:10.1016/j.jsv.2007.05.036.

[24] Z. Tong, J. He, H. Jiang, G. Duan, Optimal design of a class of generalized symmetric Gough-Stewart parallel manipulators with dynamic isotropy and singularity-free workspace, Robotica 30 (2) (2012) 305–314. doi:https://doi.org/10.1017/S0263574711000531.

[25] H.-Z. Jiang, J. feng He, Z.-Z. Tong, W. Wang, Dynamic isotropic design for modified Gough-Stewart platforms lying on a pair of circular hyperboloids, Mechanism and Machine Theory 46 (9) (2011) 1301–1315. doi:https://doi.org/10.1016/j.mechmachtheory.2011.04.003.

[26] Y. P. Singh, N. Ahmad, A. Ghosal, Design of decoupled and dynamically isotropic parallel manipulators considering five degrees-of-freedom, Journal of Mechanisms and Robotics 16 (1) (Apr. 2023). doi:10.1115/1.4062176.

[27] A. Ghosal, Robotics: Fundamental Concepts and Analysis, Oxford, 2006.

[28] Y. P. Singh, N. Ahmad, A. Ghosal, Design of Dynamically Isotropic Modified Gough- Stewart Platform Using a Geometry-Based Approach, in: Advances in Asian Mechanism and Machine Science, Springer, 2021, pp. 258–268. doi:https://doi.org/10.1007/978-3-030-91892-7_24.

[29] A. K. Mallik, S. Chatterjee, Principles of Passive and Active Vibration Control, East-West-Press, New Delhi, 2014.